Classical and Quantum Gravity

PAPER • **OPEN ACCESS**

Ar transport and blister growth kinetics in titania-doped germania-based optical coatings

To cite this article: Émile Lalande *et al* 2024 *Class. Quantum Grav.* **41** 115013

OPEN ACCESS
IOP Publishing
Classical and Quantum Gravity
Class. Quantum Grav. **41** (2024) 115013 (30pp)
https://doi.org/10.1088/1361-6382/ad3ffb

Ar transport and blister growth kinetics in titania-doped germania-based optical coatings

Émile Lalande[1], Aaron Davenport[2], Lory Marchand[2], Ashot Markosyan[3], Daniel Martinez[4], Annalisa Paolone[5,6], Michael Rezac[4], Marco Bazzan[7,8], Martin Chicoine[1], Julien L Colaux[9], Matthieu Coulon[10], Martin M Fejer[3], Alexandre W Lussier[1], Ettore Majorana[6,11], Ludvik Martinu[12], Carmen Menoni[2], Christophe Michel[10], Fulvio Ricci[6], François Schiettekatte[1,*], Nikita Shcheblanov[13], Joshua R Smith[4], Julien Teillon[10], Guy Terwagne[9] and Gabriele Vajente[14]

[1] Département de physique, Université de Montréal, Montréal, QC H3C 3J7, Canada
[2] Department of Electrical and Computer Engineering, Colorado State University, Fort Collins, CO 80523, United States of America
[3] Edward L. Ginzton Laboratory, Stanford University, Stanford, CA 94305, United States of America
[4] The Nicholas and Lee Begovich Center for Gravitational-Wave Physics and Astronomy, California State University, Fullerton, CA, United States of America
[5] Consiglio Nazionale delle Ricerche, Istituto dei Sistemi Complessi, Piazzale Aldo Moro 5, 00185 Roma, Italy
[6] Istituto Nazionale di Fisca Nucleare, Sezione di Roma, Piazzale Aldo Moro 5, 00185 Roma, Italy
[7] University of Padova, Department of Physics and Astronomy, Via F. Marzolo 8, 35131 Padova, Italy
[8] Istituto Nazionale di Fisica Nucleare, Sezione di Padova, Padova, Italy
[9] Laboratoire d'Analyse par Réactions Nucléaires (LARN), Namur Institute of Structured Matter (NISM), Université de Namur, Namur, Belgium
[10] Laboratoire des Matériaux Avancés - IP2I, CNRS, Université de Lyon, Université Claude Bernard Lyon 1, F-69622 Villeurbanne, France
[11] Sapienza University of Rome, Department of Physics, Piazzale Aldo Moro 5, 00185 Roma, Italy
[12] École Polytechnique de Montréal, Montréal, QC H3C 3A7, Canada

[*] Author to whom any correspondence should be addressed.

[13] Laboratoire Navier, École des Ponts, Université Gustave Eiffel, CNRS, F-77420 Marne-la-Vallée, France
[14] LIGO Laboratory, California Institute of Technology, Pasadena, CA 91125, United States of America

E-mail: francois.schiettekatte@umontreal.ca

Received 14 October 2023; revised 12 March 2024
Accepted for publication 17 April 2024
Published 9 May 2024

Abstract

Blistering is a phenomenon sometimes observed in sputtered-deposited thin films but seldom investigated in detail. Here, we consider the case of titania-doped germania (TGO)/silica multilayers deposited by ion beam sputtering. TGO is a candidate as high refractive index material in the Bragg mirrors for the next iteration of gravitational waves detectors. It needs to be annealed at 600 °C for 100 h in order to reach the desired relaxation state. However under some growth conditions, in 52-layer TGO/silica stacks, blistering occurs upon annealing at a temperature near 500 °C, which corresponds to the temperature where Ar desorbs from TGO. In order to better understand the blistering phenomenon, we measure the Ar transport in single layers of TGO and silica. In the case of <1 μm-thick TGO layers, the Ar desorption is mainly limited by detrapping. The transport model also correctly predicts the evolution of the total amount of Ar in a 8.5 μm stack of TGO and silica layers annealed at 450 °C, but in that case, the process is mainly limited by diffusion. Since Ar diffusion is an order of magnitude slower in TGO compared to silica, we observe a correspondingly strong accumulation of Ar in TGO. The Ar transport model is used to explain some regimes of the blisters growth, and we find indications that Ar accumulation is a driver for their growth in general, but the blisters nucleation remains a complex phenomenon influenced by several other factors including stress, substrate roughness, and impurities.

Keywords: blistering, argon, annealing, thermal desorption, ion beam analysis, scatterometer, bragg reflector

1. Introduction

Accumulation of implanted gas atoms and molecules in inorganic materials is known to result in bubbles and blistering, especially when the material is heated. Cases range from α particles emitted by fission reactions forming He bubbles in the nuclear fuel [1] to H implanted in plasma-facing materials in tokamaks, resulting in their degradation [2], to H blistering of crystalline silicon (c-Si) [3] at the basis of the SmartCut® process [4], and revealing a complex interplay with point defects and impurities [5, 6]. Related to the aforementioned subjects, there is a large body of literature on blistering following gas ion implantation in order to understand the phenomenon. However there are much fewer reports on blistering occurring as a result of gas being incorporated in the material during deposition by techniques such as ion beam

sputtering (IBS), magnetron sputtering (MS) or atomic layer deposition. Examples of blistering during annealing of single layers deposited by such technique are described in [7–9]. One recent and detailed study is that of Hatton *et al* [10] on Ar and Xe clustering in cadmium telluride deposited by pulsed MS, where blisters appear during an activation annealing at 400 °C. In such a case, the question arises whether blistering is initiated by stress-induced cracking, or gas accumulation, or a synergistic combination of both.

Here we investigate the case of blistering in multi-layer amorphous structures deposited by IBS using an Ar beam, a phenomenon observed during the development of a Bragg reflector consisting in quarter-wavelength layers of $Ti_{0.44}Ge_{0.56}O_2$ (TGO [11], high refractive index) alternated with SiO_2 (low index). These materials and structure are being developed in the context of gravitational wave detectors (GWDs) Advanced LIGO [12] and Advanced Virgo [13]. Current GWDs are able to detect the fusion of black holes [14] and neutron stars [15], but at present, the main source of noise in the most sensitive frequency range of these detectors is the thermal noise [16]. Through the fluctuation-dissipation theorem [17], this noise finds its origin in the internal mechanical dissipation (IMD) [18], a peculiar phenomenon especially significant in amorphous materials: because they can reconfigure, amorphous materials absorb mechanical energy through such reconfiguration, hence correspondingly produce mechanical fluctuations. TGO has recently been identified as a prime candidate for the next Advanced LIGO/Virgo mirrors, as it shows low IMD when annealed at 600 °C for 100 h, while featuring a relatively high refractive index [11].

Blistering sometimes appeared in such multi-layer stacks upon annealing at around 500 °C. The main factor was eventually found to be a non-optimal base vacuum (lower 10^{-6} torr) resulting from a small water leak in the IBS system. The repair allowed to reach a base vacuum in the lower 10^{-7} torr, and very few or no blisters were observed in the annealed stacks afterwards. However the phenomenon also appears in other experiments, and its occurrence seems to depend on several factors, such as the number of layers, the substrate roughness, and the stress in individual layers, all of which are being optimized to avoid this effect [19].

Thanks to a new setup allowing imaging during annealing [20], we are able to observe the growth of the blisters as a function of temperature and time in such stacks, then link it to the desorption and transport kinetics of the Ar incorporated into the TGO layers during deposition, providing an opportunity to better understand the phenomenon. While the nucleation of the blisters is likely driven by stress, surface roughness or adhesion affected by water vapor, we show that their growth occurs at the same temperatures at which Ar is released from TGO. In some stacks, we show that blister growth happens in a two-step process: a fast initial growth followed by a growth controlled by thermally activated Ar detrapping. We also observe a significant accumulation of Ar in the TGO layers, which occurs because Ar diffusion is much slower in TGO than in SiO_2. This likely plays an important role in the blistering process.

2. Experimental methodology

2.1. Substrates and deposition

SiO_2 and TGO single layers and TGO/SiO_2 stacks were grown by IBS deposition on two different systems. Single layer samples are listed in table 1. Samples #0 to #3 were deposited using a Veeco Spector DIBS system in the Engineering Research Center at Colorado State University (CSU). The system was baked at 150 °C and pumped to a base pressure of 5–20 $\times 10^{-7}$ Torr prior to deposition. The upper bound was during a period where a small water leak in the source cooling system occurred, and most of the residual gas was water vapor, as confirmed by mass spectrometry. The system chamber temperature was set to 60 °C during

Table 1. Annealing schedules of samples bearing a single layer and deposited during the indicated run. For most samples, a piece of the same sample was annealed only once, for the indicated time and temperature, except for samples #0 and #1 where the same piece was annealed at 300 °C for 10 h, then characterized by RBS, then annealed a second time at the next indicated temperature for another 10 h, reanalyzed, and so on. While most samples were annealed for a fixed duration at different temperatures, different pieces of sample #3b were annealed at a fixed temperature (600 °C) for different times. Samples #4b, 5 and 6 were used for TDMS measurements, which were conducted in vacuum.

#	dep. run	Material	thick. (nm)	Time	Gas	Temperatures (°C)
0	210526a	SiO_2	225	10 h × 4	air	300, 300*, 400, 450
1	210216a	TGO	321	10 h × 6	air	300, 300*, 400, 450, 450*, 500
2	210928a	TGO	217	20 h	N_2	400, 450, 500
3a	211106a	TGO	250	10 h	air	200, 300, 400, 500, 600, 700
3b	211106a	TGO	250	250 s, 500 s, 1000 s	N_2	600
4a	C22047	TGO	80	20 h	N_2	400, 450, 500
4b	C22047	TGO	80	TDMS	vacuum	ramp 3 °C min^{-1}
5	C23028	TGO	558	TDMS	vacuum	ramp 3 °C min^{-1}
6	C22034	TGO	1000	TDMS	vacuum	ramp 3 °C min^{-1}

*Annealed in N_2:O_2.

depositon. The radiofrequency (RF) ion source was operated with Ar as the process gas, with 1500 V applied on the exit W grid and an integrated beam current of 300 mA. A Ge target was masked with a Ti sheet to give a Ti/Ge cation ratio of 44/56. In the case of stacks, the target was switched to a Si target. In order to form stoichiometric oxides, a flow of O_2 (49 sccm) was introduced in front of the target and 21 sccm of O_2 was introduced through a secondary RF ion source, also producing an energetic source of oxygen ions. During deposition, the pressure was 0.42 mTorr.

Samples #4-6 were deposited using a custom IBS system at Laboratoire des Matériaux Avancés. The system was baked at 120 °C and pumped to a base pressure of 2×10^{-6} Torr prior to depositions. The 16 cm RF ion source was operated with Ar flowing at 20 sccm and an integrated beam current of 300 mA. The targets consisted of a Ti plate and a Ge plate. The position of the target holder was adjusted in front of the beam of the ion source to provide a Ti/Ge cation ratio of 44/56. In the case of stacks, the target holder was switched to a SiO_2 target. In order to form stoichiometric oxides, a flow of O_2 (75 sccm for TGO, 25 sccm for SiO_2) was introduced in front of the targets. During deposition, the pressure was 3×10^{-4} torr.

The single layers were measured by spectroscopic ellipsometry (Horiba UVISEL) and the measurements were modeled to extract the refractive index and thickness. Thicknesses are reported in table 1.

2.2. Isothermal annealing

Annealing at Université Montréal (UdeM) was carried in a Minibrute furnace under a gas flow of 500 sccm of N_2 at atmospheric pressure. The furnace temperature was calibrated by inserting a thermocouple inside the furnace quartz tube and measuring the temperature at several temperature settings on the furnace. Pieces of samples #2 and #4a were inserted in the furnace which was turned on and took 30 min to reach the desired temperature, where they remained for 20 h. The furnace was then turned off to cool down on its own to room temperature (RT). Pieces of sample #3b were annealed at higher temperature for a few minutes, in which case the

samples were introduced in less than 5 s into the furnace after its temperature had stabilized, and were also removed in less than 5 s at the end of the annealing time.

At CSU and Stanford University (Stanford), the samples were placed in a furnace with an air atmosphere to be heated at rate of 1.5 °C min^{-1}, until it reached the desired temperature, and then cooled at a rate of 1.5 °C min^{-1} until 40 °C.

Annealing both in air and a mix of N_2:O_2 were performed at Stanford following similar annealing schedules. The latter gas was used to see if the absence of the 1% Ar present in air has an effect on Ar content in the layer. We could not observe any effect within the sensitivity of the depth profiling technique. In addition, these anneals were carried out sequentially on the same samples, while being depth-profiled by ion beam analysis (IBA) at UdeM between each annealing. The different annealing conditions considered in this study for single layers are reported in table 1.

2.3. Thermal desorption mass spectrometry

Thermal desorption mass spectrometry (TDMS) was performed in Rome using a system composed of an MTI GSL100 vacuum furnace equipped with a quartz tube, connected to a Pfeiffer Vacuum QMS200 mass spectrometer. The base pressure inside the tube was of the order of 10^{-7} Torr. Scanning measurements were conducted with a temperature rate of 3 °C min^{-1} while monitoring the Ar partial pressure.

2.4. Imaging during annealing profile

To learn more about the formation and growth of blisters in the coatings, *in situ* scattered-light imaging of the samples during selected annealing profiles was performed using the Air Annealing Scatterometer at California State University, Fullerton [20]. This setup consists of a programmable industrial annealing oven (Sentrotech ST-1500C-121012) which was modified to add instrument flanges and viewports through the outer walls and insulation allowing observation of the oven's interior during annealing. The maximum temperature our setup can reach is 900 °C–1100 °C. The temperature is read by an S-type thermocouple that is located in the air a few inches from the sample. The oven's temperature controller (Eurotherm Nanodac) allows custom heating profiles and includes proportional-integral-derivative control.

Each sample was mounted in a custom stainless steel holder. A superluminescent diode (SLD, Thorlabs SFC1050P) with long coherence length ≈20 μm, to avoid coherent effects such as twinkling) was used to illuminate the samples at 1050 nm (close to the wavelength used by the Advanced LIGO and Advanced Virgo observatories, 1064 nm). A single ($f = 200$ mm) converging lens and adjustable iris cast an image of the optical sample (with magnification $M = 2$) onto a low-noise and high-resolution silicon CCD camera (4096×4096 pixel Apogee Alta F16M) field of view in the object plane of height 1.83 cm and a viewing angle from the normal of the sample of $\theta_s = 8°$.

A LabView Virtual Instrument (VI) is used to automate the control and data acquisition of the oven, SLD, and camera. To set up a typical run, a pre-cleaned sample is installed and the image is focused on the camera so that the image plane is at the sample's surface. Then the desired heating profile is loaded to the oven's controller and the desired camera exposure time (5 seconds for these runs) and imaging cadence are entered into the VI. The oven and VI are started and data is collected in the sequence: (i) read oven set point and thermocouple temperature; (ii) turn on SLD; (iii) bright image exposure and transfer image; (iv) turn off SLD; (v) dark image exposure and transfer image; (vi) wait until desired cadence time; repeat until user selected stopping point. The images are stored in the flexible image transport format.

Blackbody radiation from the oven and its heaters becomes a dominant source of light at higher annealing temperatures. To combat this, the camera has an attached tube with a narrowband filter (Edmunds 1050 nm/50 nm) attached to its entrance to filter out radiation far from the SLED wavelength. In addition, 'dark' images taken with the SLED turned off can be subtracted from 'bright' images with the laser on to reduce the influence of blackbody radiation on the images. However, for the analyses below, the blackbody radiation from the oven's heating elements (after passing the narrowband filter on the camera) was found to be the most effective illumination channel for observing blister formation and dynamics (also discussed in [20]). This acts similarly to side or back illumination in microscopy and allows a clear view of the blister shape. So below we present data made entirely from 'dark' images without SLED illumination.

2.5. Blister profiling

Pictures of blisters in a 52-layer coating of GeO_2:TiO_2/SiO_2 were taken using an OLYMPUS IX71 optical microscope, equipped with a mercury lamp and a green filter. The wavelength of the light was set to around $\lambda = 550$ nm. An intensity line out from the edge to the center was taken for each blister in MATLAB, to determine the position of the dark and bright fringes and calculate the height of a blister as a function of the base radius.

When large blisters are observed under the microscope, a circular interference pattern is produced by the internal reflection of the light between the base and the curved top surface of the blister. The position of the bright and dark fringes of these Newton's rings can then be used to calculate the thickness at any point across the blister. Starting from the edge, the thickness along the nth bright fringe is equal to $n\lambda/2$ and the mth dark fringe corresponds to a height of $(m + 0.5) \times \lambda/2$.

2.6. Ion beam analysis

Rutherford backscattering spectrometry (RBS) was carried out on a 1.7 MV Tandetron accelerator at UdeM using a He beam to determine the composition and the areal atom density of the TGO and SiO_2 single layers deposited on witness crystalline Si samples. A 4.5 MeV He beam was used on the TGO layers in order to resolve the contribution of Ti, Ge, and Ar. All single layer samples were also analyzed using a 2 MeV He beam as to avoid nuclear resonances and to be able to rely on the Rutherford cross-section to determine the amount of oxygen. The incidence angle of the beam with respect to the surface normal was 7° in order to avoid channelling in the Si substrates, and the detector was placed at a scattering angle of 170° to maximize the mass resolution. In order to determine the areal atomic density and the composition, measurements were compared to simulations carried out using SIMNRA [21]. The Ar peaks from the RBS spectra obtained from single layers were further converted into depth profiles by simply assuming that, for the as-deposited samples, the half-height of the Ar peak on the high-energy side is at the surface, and that the half-height of the same peak on the low-energy side is at a depth corresponding to the layer thickness as determined by ellipsometry. A linear background was also fitted to the channels on the low-energy side of the peak, and subtracted from the spectra. In depth profiles presented here, the origin of the depth axis is at the surface of the sample.

RBS could not be used to depth profile $<1\%$ of Ar in 52-layer stacks as they are fairly thick (8.5 μm) and because the Ti and Ge peaks (seen in figure 1 for a single layer) completely overlap and obscure the Ar contribution to the spectrum. Instead, we used both elastic

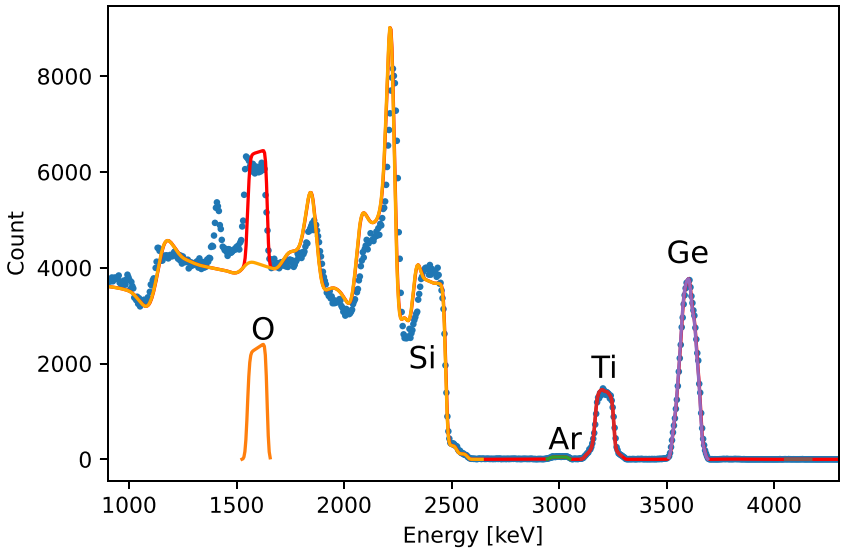

Figure 1. RBS spectrum acquired from sample #2 by means of a 4.5 MeV He beam (dots), and compared to a SIMNRA simulation (red curve). The contribution of the different elements to the simulation appears in different colors and are identified by their symbol.

recoil detection with a time-of-flight detector (ERD-TOF), and particles induced x-ray emission (PIXE).

ERD-TOF was carried out on the 6 MV Tandem accelerator at UdeM [22] where the beam is incident at 15° from the surface, and the TOF detector is located at 30° from the beam axis. The measurements were carried out using Cu and Si beams, both at 50 MeV. The former gives a spectrum for all elements present with concentration $>0.1\%$ (H, O, Si, Ar, Ti and Ge), but the depth of probe is limited to the first 2.5 layers of our stacks, while the latter allows us to probe down to the 5th or 6th layer, depending on the element, as Si features a lower stopping cross section and provides a high energy transfer on Ar, Ti and O. This is at the expense of obtaining a Si recoil spectrum, however. Energy spectra were converted into depth profiles using the Allegria software [23].

Conversely, PIXE allows us to probe the total amount of Ar through a complete stack, but without any depth resolution. These measurements were carried out at the University of Namur on a 2 MV Tandetron accelerator using a proton beam of 2.5 MeV. The x-ray detector was placed at 135° from the incident beam. A 6 μm Al foil absorber was placed in front of the LEGe detector to reduce the pile-up signal from Si, and could have interfered with Ar x-ray signal. The samples were measured at two different angles: normal incidence and 45°. The simulation software GupixWin was used to analyze the resulting x-ray spectra and extract the total Ar content [24].

3. Ar transport in Ti-doped germania

First, we report on the Ar desorption from single layers as measured by IBA and TDMS, which then serves to understand the process in stacks. Although desorption from TGO is mainly limited by detrapping in <1 μm single layers, we show that in stacks of several μm, diffusion

plays an important role. Through a finite element model, we show that the observed accumulation of Ar in TGO can be explained by its slower diffusion in that material compared to silica.

3.1. Depth profiling of Ar desorption from single layers

RBS spectra were acquired from single layer samples #0, #1, #2 and #4a after each annealing (see table 1). Figure 1 shows an example of the spectrum (dots) measured with a 4.5 MeV He beam on sample #2 before annealing. The peaks corresponding to the different elements are identified. The solid red curve is a SIMNRA simulation considering a layer of 1.5×10^{18} at cm^{-2} consisting of 15.0% Ti, 17.5% Ge, 67% O, 0.7% Ar and 0.01% W, on top of an Si substrate. The contribution of the signal of each element to the spectrum is shown with curves of different colors, most of which overlap the red curve except that of oxygen, which shows up on top of the Si signal. The W is an impurity commonly found in such layers, and originates from some sputtering of the acceleration grid in the ion beam source of the IBS system. The same applies to the amount of Ar observed, which is incorporated as Ar ions from the IBS beam source are scattered by the Ti:Ge target and impinge the surface of the deposited layer throughout the process. Because there is a small amount of Ar, a higher beam energy is required during the RBS measurements to resolve the Ar peak from the neighboring Ti peak. The acquisition time was long enough to achieve sufficient statistics in order to extract Ar depth profiles that reveal the desorption kinetics. As a consequence of the choice of beam energy, the cross section of the collisions with Si features several non-Rutherford nuclear resonances. Differences with the simulation can be due to some surface charge-up (as TGO is an insulating material) or slight departures from the beam energy, stopping power and angle compared to the cross-section estimated by SigmaCalc [25]. (A peak present at 1.4 MeV is due to the protons coming out of a $^{28}\mathrm{Si}(\alpha,\mathrm{p}_0)^{31}\mathrm{P}$ nuclear reaction [26].) For these reasons, measurements were also carried out using a 2 MeV beam to ensure a precise estimate of the elements concentration. This is also the energy used to depth-profile Ar in the silica single layer (sample #0), for which the Ar peak does not suffer from the Ti peak overlap.

The part of the RBS spectra acquired at 4.5 MeV which correspond to Ar is shown as solid broken lines in figure 2 for samples as deposited, and annealed at temperatures indicated on the figures for times reported in table 1. The energy scale of the spectrum is converted to a depth scale according to the method described in section 2.6. The depth profiles are broadened by the detector resolution and other effects, which is why a part of the profiles show up at negative depths. The broadening is relatively large, owing to the choice of energy to resolve the Ar peak. As He ions of such energy suffer a relatively low energy loss, a given energy resolution translates into a relatively large depth.

Yet, the resolution is sufficient and statistical fluctuations are low enough, despite the weak signal, to observe that in thicker layers (top three panels of figure 2 the depth profiles of as-deposited samples feature a uniform Ar concentration, while the Ar depth profiles become non-uniform upon annealing, with less Ar closer to the surface. In the case of Ar in silica (top panel), the desorption process occurs over 150 °C, while in TGO (bottom three panels), most of the desorption occurs on a relatively limited temperature range, between 450 °C and 500 °C. We will see that the former is well modeled by a diffusion process, while the latter is compatible with a detrapping-limited mechanism, but the fact that some depth profiles are non-uniform means that the desorption might be in part limited by diffusion.

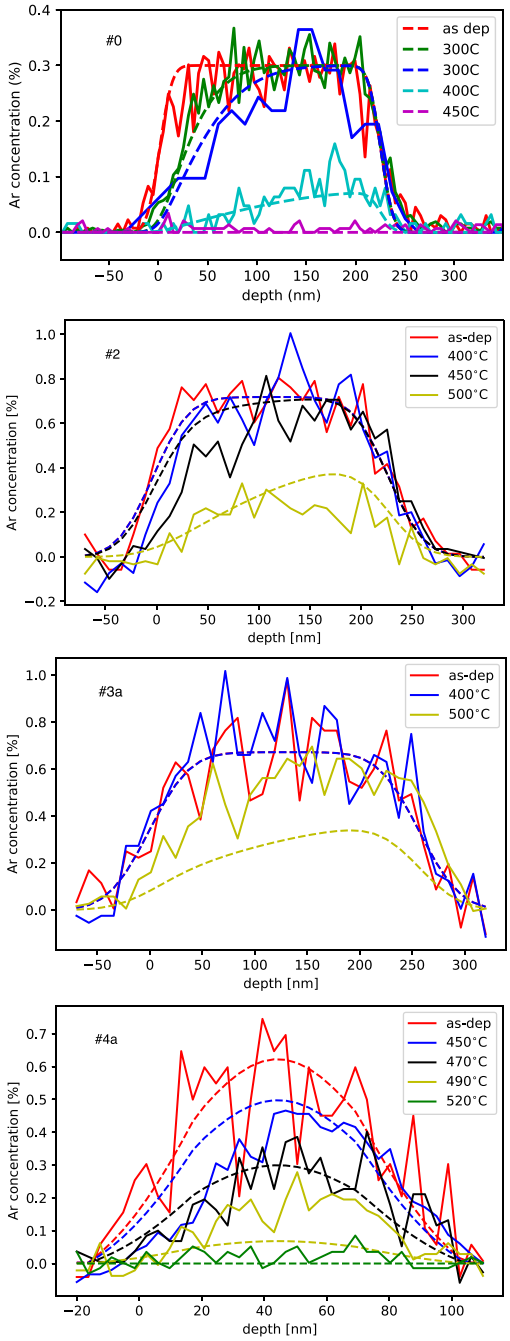

Figure 2. Ar peak from the RBS spectra acquired at 4.5 MeV on single layers number indicated on each panel, for as-deposited samples (as-dep) and annealed at indicated temperatures for the time shown in table 1. The horizontal energy scale of the Ar spectrum is converted to a depth scale following the method summarized in section 2.6. Broken solid lines: experimental data. Dashed curves: transport model. Note the different depth scale for each panel.

3.2. Ar desorption kinetics in single layers

Many processes can limit desorption. Here, we model the data with two such processes: diffusion and detrapping. The latter means that Ar atoms are initially trapped, for example in substitutional sites, and need to escape such a location in order to start diffusing to eventually reach the surface and desorb. It could be argued that a substitutional site is an ill-defined concept in an amorphous material. But during deposition, the other atoms should end up in locations that leave enough room for the Ar atoms in order for them to be incorporated when a new surface is forming, and the material should relax in such an Ar-accommodating configurations. Then, upon annealing, Ar atoms, which are not covalently bond as the other atoms in the oxide, may escape their location more easily, but to a location where the (now bulk) material cannot accommodate them without significant local mechanical deformation, similar to an interstitial in a crystal. And as for interstitials in crystals, this also means that they can now diffuse with lower energy barriers. If such diffusion is fast at the annealing temperature where the atoms were detrapped and the distance to the surface is short, then the desorption process is only limited by detrapping. Conversely, if the barrier is low to jump out of the trapping site, then the desorption process might be only limited by diffusion. Another process often considered in desorption kinetics is surface adsorption, but because Ar is a rare gas, this is very unlikely to be a limiting process at RT and above. In addition, it would lead to a barrier at the surface, favoring a constant concentration through the layer, contrary to what we observe. Here, we compare the experimental depth profiles to a model that includes both detrapping and diffusion as follows.

Assuming that detrapping is a thermally activated process with a single activation energy E_A, since it occurs at a rate proportional to the atom density N of Ar still trapped, we have

$$\frac{\mathrm{d}N}{\mathrm{d}t} = -N\,\nu_0 e^{-E_\mathrm{A}/k_\mathrm{B}T}, \tag{1}$$

where ν_0 is an attempt frequency typical of vibrations in such solids, which we take as 10^{13} Hz. The Boltzmann factor (in which k_B is the Boltzmann constant) gives the probability that a detrapping attempt is successful. For isothermal annealing at temperature T for time t, the solution to this equation is

$$N(t) = N_0 \exp\left(-\nu_0 t e^{-E_\mathrm{A}/k_\mathrm{B}T}\right), \tag{2}$$

where N_0 is the Ar content at $t = 0$. This expression can be used directly to fit the evolution of the total Ar content in the experiments shown in the previous subsection if the desorption process is only limited by detrapping.

The symbols in figure 3(a) show the remaining Ar total content in three samples bearing a TGO single layer as a function of annealing temperature. The curves represent equation (2) in which the annealing time comes from the values in table 1. In the case of sample #1, since the annealings were conducted in sequence on the same sample, the concentration $N(t = 10\,\mathrm{h})$ calculated at the end of the previous anneal is used as N_0 for the next. A least squares fit is carried out for all data simultaneously in order to find the best fitting value for E_A, which is 2.75 eV. The model shows excellent agreement with the data, which would point towards the conclusion that Ar desorption from TGO is only limited by detrapping.

However, we have already mentioned that the shape of the Ar depth profile upon annealing implies that diffusion is also involved. Indeed, if diffusion is not a limiting process, i.e. if it is fast enough not to come into play in the desorption process, the depth profiles would remain

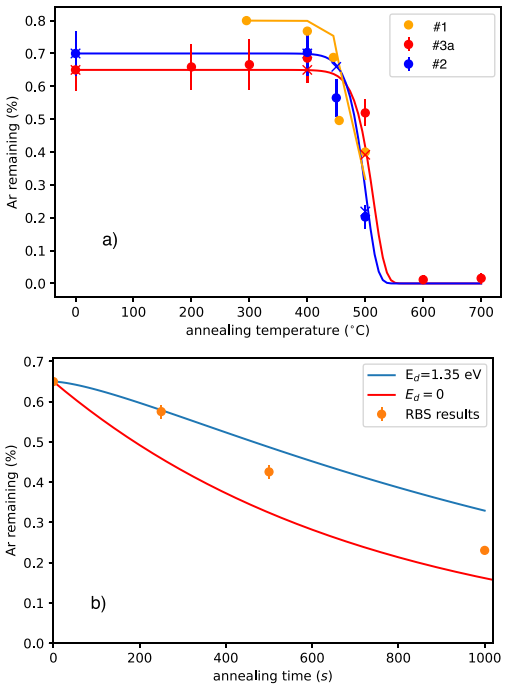

Figure 3. (a) Total amount of Ar remaining in indicated TGO samples as a function of annealing temperature. Curves: equation (2) with $E_\mathrm{A} = 2.75$ eV. Symbols $\times$ show the total amount of Ar remaining in sample #2 and #3a considering the numerical model (equation (4)) with $E_\mathrm{A} = 2.70$ eV and $E_\mathrm{D} = 1.35$ eV. (b) Symbols: total amount of Ar remaining in sample #3b as a function of annealing time at 600 °C. The red curve is the expected concentration considering equation (2) with $E_\mathrm{A} = 2.75$ eV (i.e. not diffusion-limited) while the blue curve is deduced from the numerical model.

flat, as the Ar atoms would quickly move in the layer and reach the surface to desorb. Another indication of the influence of diffusion on the desorption process is found in figure 3(b), which shows the total amount of Ar remaining in sample #3b as a function of time after anneals at 600 °C (symbols). On this graph, equation (2) is plotted as a red curve, and is essentially a decreasing exponential. This is not the case of the experimental points, and we see that the model does not represent the data very well.

So we now include diffusion in our model. Let $C(x,t)$ be the detrapped density of Ar atoms at depth x and time t. According to the second Fick's law [27],

$$\frac{\mathrm{d}C}{\mathrm{d}t} = \frac{\mathrm{d}}{\mathrm{d}x}\left(D\frac{\mathrm{d}C}{\mathrm{d}x}\right) - \frac{\mathrm{d}N}{\mathrm{d}t}, \tag{3}$$

where the last term is a source term corresponding to the rate of Ar atoms released from their trap, equation (1). In equation (3), D is the diffusion coefficient, which we consider again to be a thermally activated process with a single activation energy E_D, so that $D = D_0 e^{-E_\mathrm{D}/kT}$. The boundary conditions are the following: we assume all Ar atoms reaching $x = 0$ are released from the target (i.e. desorbs), so $C(x = 0, t) = 0$. We also assume that the interface is a perfect

reflector, i.e. that atoms reaching the interface at depth L simply go in the other direction, i.e. $\mathrm{d}C(x=L,t)/\mathrm{d}x=0$. Equation (3) cannot be solved analytically in our case, so we integrate it numerically as follows:

$$\begin{aligned} C_{t+\Delta t}[x] = C_t[x] + (F[x-\Delta x] \times C_t[x-\Delta x] - 2F[x]\,C_t[x] \\ +F[x+\Delta x]\,C_t[x+\Delta x])\,\Delta t + N[x]\;\nu_0 e^{-E_\mathrm{A}/k_\mathrm{B}T}\Delta t, \end{aligned} \tag{4}$$

where $C_t[x_i]$ is the concentration C at a time t and depth x_i and F is defined as:

$$F[x] = D[x]\,\frac{\Delta t}{\Delta x^2} \tag{5}$$

which depends on the diffusion coefficient in the different materials (TGO and SiO_2) and where ΔT and Δx are the time and position steps during the integration. At $t=0$, $N[x_i]=N_0$ for $0<x_i<L$ and decreases with time by the amount corresponding to the last term of equation (4). The boundary conditions are applied by setting $C_t[0]=0$ and $C_t[L]=C_t[L-\Delta x]$.

For silica, according to the literature [28], desorption is only limited by diffusion with coefficients $D_0=10^{-5.06}$ cm^2/s and $E_\mathrm{D}=1.2$ eV. Using these values, and assuming that all Ar atoms are detrapped and diffusing (i.e. $C(x)=N_0$ and $N(x)=0$ at $t=0$), we solve equation (4) considering sample #0. Results are reported as dashed curves in the top panel of figure 2. We see that the model is in very good agreement with the data. We therefore do not further optimize these coefficients.

For Ar in TGO, we need to include both detrapping and diffusion to reproduce the evolution of the depth profiles. Since the desorption occurs on a limited temperature range, it is difficult to find reliable values for both D_0 and E_D in the same fit, as they compensate each other. Rather, we set D_0 to a constant value, the same as for silica from [28], which is typical of the diffusion coefficients in several materials, and is of the order of magnitude of atomic steps at frequency ν_0.

Then, in order to determine the values of E_A and E_D that best fit the experimental Ar depth profiles $R(x_j)$ from the bottom three panels of figure 2 (broken lines), we compute the least squares with the ones obtained numerically from the model (i.e. $C_t(x_i)$ at temperatures and after a time t indicated in table 1) as follows:

$$S = \sum_{\text{profiles}} \sum_{x_j} \left(\tilde{C}_t(x_j) - R(x_j)\right)^2, \tag{6}$$

where $\tilde{C}_t(x_j)$ is $C_t[x_i]$ convoluted for the experimental depth resolution. Also, Δx during the computation of the transport model is much smaller than the interval between the points in the experimental depth profiles $R(x_j)$, so the values of $\tilde{C}_t(x_i)$ are interpolated at points x_j of the experimental depth profiles in order to compute equation (6).

The reciprocal of this equation, $1/S$, is plotted as a function of both E_A and E_D in figure 4, so the best fit is for the highest value. The top panel is for thicker layers, samples #2 and #3a, for which the depth profiles are presented in the corresponding panels of figure 2. Figure 4(b) considers the thinner layer (sample #4a), for which the depth profiles are presented in the bottom panel of figure 2. If we now consider all the Ar depth profiles for samples #2, #3a and #4a in figure 2, the bottom panel of figure 4 indicates that the best overall agreement is found for E_A and E_D of 2.70 eV and 1.35 eV, respectively. We also see that the value of E_D is not well constrained and could be smaller, with E_A slightly larger.

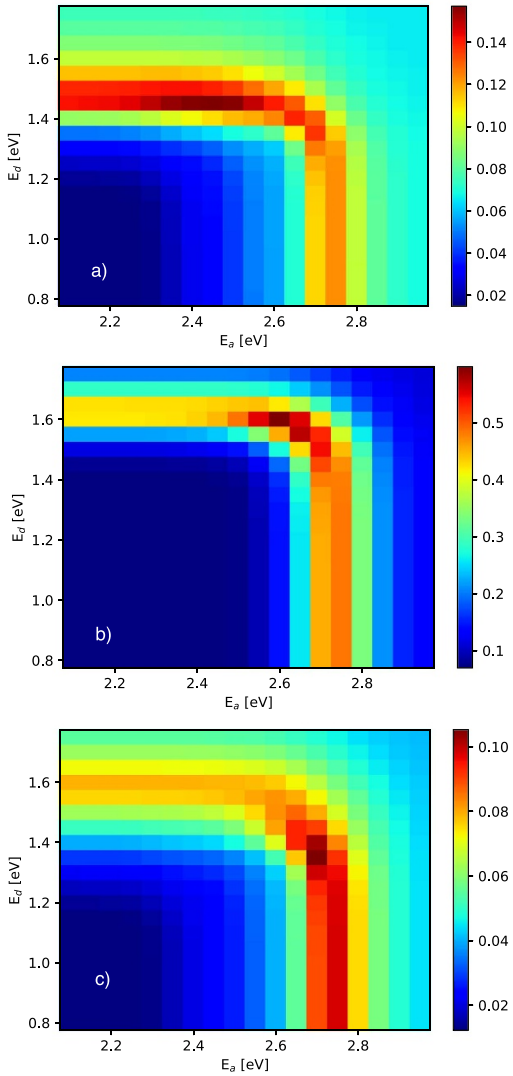

Figure 4. Maps of $1/S$ as a function of the activation energy for diffusion (E_{D}) and detrapping (E_{A}). The darkest spots denote the best agreement between the experimental data and the model. (a) Map considering the Ar depth profiles of annealed samples #2 and #3b (TGO layer >200 nm thick) shown in the corresponding panels of figure 2. (b) Map considering the Ar depth profiles of annealed sample #4a (80 nm) as shown in the bottom panel of figure 2. (c) Map obtained when including all the Ar depth profiles in TGO.

The curves $\tilde{C}_t(x_i)$, considering this optimal overall solution, are plotted as dashed curves in figure 2 for samples #2, #3a and #4a. We see from the figure that the model agrees in general with the data, with some discrepancies where the experimental data are lower than predicted by the model. This usually happens over the short temperature intervals during which the detrapping happens. This means that changes in E_{A} smaller than the uncertainty would result in a better agreement.

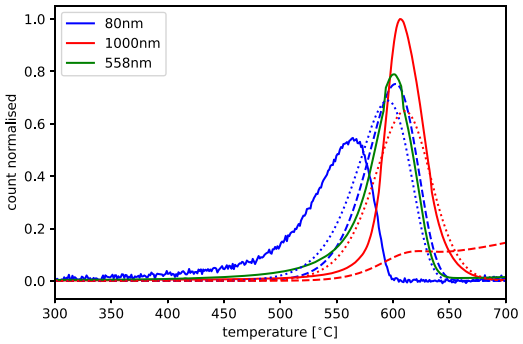

Figure 5. TDMS measurements and models for sample #4b (blue), #5 (green) and #6 (red), normalized to their thickness. Solid curves: TDMS results. For samples #4b and #6 samples only, the dashed curves represent the model considering $E_D = 1.35$ eV and $E_A = 2.70$ eV as found in section 3.2, while the dotted curves consider the model assuming a detrapping-limited process (equation (2)) with $E_A = 2.75$ eV.

3.3. TDMS

TDMS is used to determine the amount of Ar desorbing as a function of temperature from single layers. This amount is shown as solid curves in figure 5 for samples #4b through #6. The data are normalized to the thickness of the deposited layer and should have the same area if the same concentration of Ar desorbs from each sample. We compare the experimental data to the model presented in the previous section (with $E_A = 2.7$ eV and $E_D = 1.35$ eV), shown as dashed curves of the same color for samples #4b and #6. We also compute the curves for a desorption process only limited by detrapping, equation (1) with $E_A = 2.75$ eV, shown as dotted lines for these two same samples. The latter reproduces reasonably well the desorption signals obtained from both the 558 nm layer (green) and the 1000 nm layer (red solid curve), but not the one from the 80 nm layer (sample #4b, blue solid curve), which peak appears at a temperature significantly lower. The model that includes diffusion (dashed curves) gives, for an 80 nm layer, a peak at a temperature similar to the detrapping-limited model, owing to the fact that diffusion is not a limiting factor for such a thin layers. In that sense, it also reproduces the signal from the 558 nm sample. However, the model with diffusion intended to reproduce the desorption from the 1000 nm layer (red dashed curve) features a long tail at higher temperatures. Since the experimental curves for the 558 nm and the 1000 nm-thick layers more or less overlap, it is an indication that, for these samples, desorption is less limited by diffusion. Yet, the shift between the two TDMS peaks is an indication that diffusion is a limiting factor. Regarding the TDMS peak for the 80 nm-thick sample (#4b), which is located at a temperature significantly lower than the other peaks, we saw in the previous subsection that the models are able to reproduce fairly well the evolution of the Ar depth profile shown in the bottom panel of figure 2. This TDMS result is therefore not well understood and appears to be an outlier.

3.4. Ar transport in stacks

We now turn to multilayer stacks, consisting of 27 TGO/SiO_2 bilayers. Each layer has an optical thickness of $\lambda/4$ at 1064 nm, except the SiO_2 top layer which is twice as thick. First,

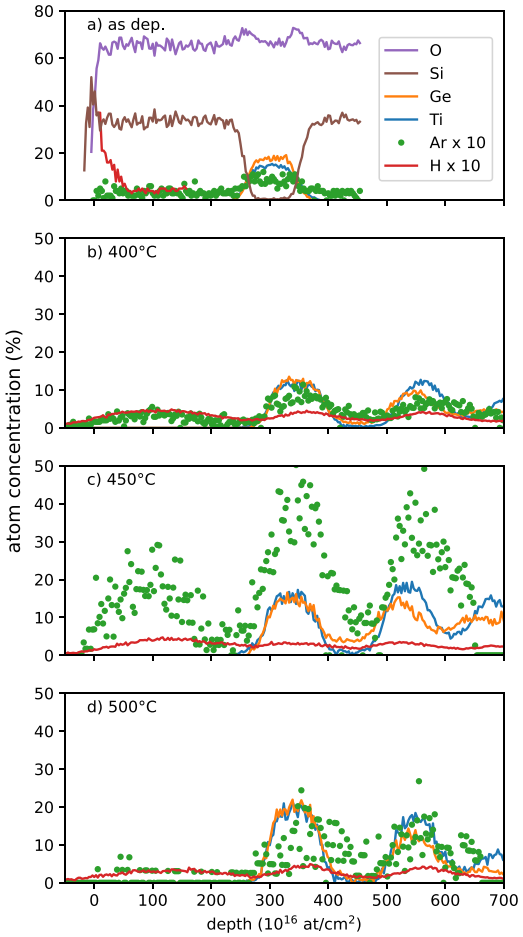

Figure 6. Concentration of the different atoms in a TGO/SiO_2 stack as a function of depth. The Ar and H depth profiles are multiplied by a factor of 10. (a) Analysis carried out using a 50 MeV Cu beam on a stack as deposited. Panels (b) through (d) show measurements performed using a 50 MeV Si beam on a stack annealed for 10 h at 400 °C, 450 °C and 500 °C, respectively. Only the Ge, Ti, Ar and H depth profiles are plotted.

we look at the Ar transport in such structure using IBA. Then, we compare these measurements to the transport model, equation (4), now applied to a full stack, using the transport coefficients found for single layers.

Figure 6 presents the depth profile of the elements in a stack obtained using ERD-TOF measurements, as deposited and annealed at indicated temperatures. The depth scale, in at cm^{-2}, can be divided by the atom density in at cm^{-3} measured by other means [29] in order to obtain a depth scale in length units. However, TGO and SiO_2 not having the same atom density, the conversion of the depth scale is not straightforward. Still, assuming an average atom density of 7×10^{22} at cm^{-2}, the maximum of the horizontal axes correspond to about 1 μm in depth.

In these graphs, the Ar and H signals are, for clarity, multiplied by a factor of 10 as their initial concentration is below 1%. The depth profiles in the top panel are obtained with a 50 MeV

Cu beam which allows to probe all the atoms that have a concentration above 0.1%, but offers depth of probe limited to the first ∼2.5 layers of the stack. On this graph, we see that the Ar content is initially about 0.3% in SiO_2 and 0.8% in TGO, that is, the same concentrations obtained by RBS in the corresponding single layers. The other atoms concentration is also the same as obtained by RBS. The oxygen profile features small bumps near the TGO/SiO_2 interfaces, but they do not show up in the energy spectra. We suggest that these bumps are rather due to an imperfect knowledge of the ions stopping power during the conversion of the energy spectra into depth profiles. These ERD-TOF measurements also reveal a H concentration of about 0.4% after a depth of 50×10^{16} at cm^{-2}. Closer to the surface, there appears to be a H contamination, possibly in part a broadened surface peak.

Then, for the annealed sample, the depth profiles are obtained using a 50 MeV Si beam, allowing to probe deeper into the stack as explained in section 2.6. Yet the depth profiles are significantly broadened by the deteriorating depth resolution, and increasingly affected by a background signal due to multiple scattering [30]. Other effects arise such as the fact that the Ti and Ge peaks do not overlap very well already in the 4th layer. This is due to an imperfect knowledge of the stopping power of both the beam ions and the recoils in such mixture. It also affects the Ar depth profile, so one must not conclude from these measurements that the Ar peaks are shifted compared to the TGO layers. Yet, they allow us to observe clear overall changes in Ar concentration in these few top layers.

In figure 6(b), we see that after an annealing at 400 °C, the Ar and H depth profiles start to feature a slightly rounded shape in the SiO_2 top layer. Actually, the Ar and H concentrations in the middle of that layer are similar to the one in the as-deposited stack, but the concentration decreases near the surface and the interface with TGO, where it reaches 0.2% for H and slightly more than 0.1% for Ar. The near-surface H peak has disappeared. In the TGO layers, the Ar concentration appears to remain similar as in the as-deposited sample, but given the uncertainty due to statistical fluctuations, it is possible that it increases slightly because of some Ar in-diffusion from the neighboring SiO_2 layers. We note that at 400 °C, Ar in SiO_2 should have started to diffuse significantly according to what is observed in figure 2 for sample #0.

Then, after an anneal at 450 °C, we see from figure 6(c) that a significant Ar accumulation occurs, with about 3.5% Ar in the TGO layers, and up to 2% in the middle of the top SiO_2 layer. In the 2nd SiO_2 layer, it reaches about 1%. At such temperature, the Ar has completely desorbed from SiO_2 single layers, and has started to detrap and diffuse out of TGO single layers (see figure 2). On the other hand, the H depth profile does not evolve significantly.

Following a 500 °C anneal, the Ar depth profile decreases down to about 0.1% in the top SiO_2 layer (i.e. close to the detection limit), and slightly below 1% in the TGO. Again, the H depth profile barely changes upon such annealing.

While ERD-TOF allows us to see the depth profile evolution, it only gives the picture of the top 10% of the stack. In order to monitor the evolution of the Ar content through the full stack, we turn to PIXE. The drawback is that we can only measure a total Ar content, with very little information about the distribution with depth. The technique is not sensitive to H. In that case, the stacks were annealed at 450 °C for up to 1000 h. We see from figure 7 that the Ar total content in the stack decreases by only 12%.

In order to understand this behavior, we apply the model of equation (4), now considering a complete stack. We use the desorption and transport parameter found in section 3.2 for single layers, that is, $E_A = 2.7$ eV $E_D = 1.35$ eV for TGO, and $E_D = 1.2$ eV for SiO_2. The model is initialized with an Ar content of 0.8% in the TGO layers and 0.3% Ar in the SiO_2, and equation (4) is computed according to the different annealing schedules. The Ar content evolution during an anneal at 450 °C is plotted as a blue curve in figure 7. We see that the

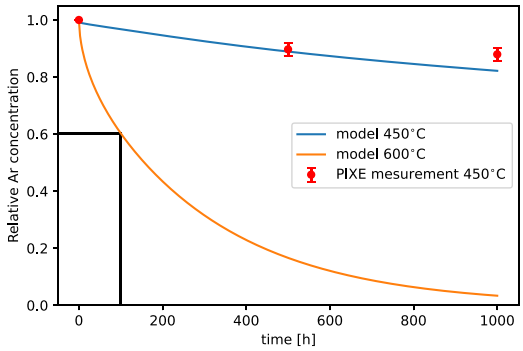

Figure 7. Symbols: Relative Ar total content as a function of annealing time at 450 °C, normalized to the yield obtained from the as-deposited sample. The blue curve shows the Ar remaining considering the diffusion-detrapping-limited model using the parameters found in section 3.2. The orange curve is the Ar remaining according to the same model if the annealing was carried out at 600 °C.

model predicts a desorption rate that compares very well to the PIXE measurements. This result reinforces our confidence in the transport parameters we determined in section 3.2.

Figure 8 shows an example of the simulated Ar depth profile after an annealing at 600 °C for 10 h. Some of the Ar in the top 2000 nm has escaped the sample, but most of it remains in the stack. Anneals much longer than 10 h would eventually result in a significant desorption, as illustrated by the orange curve in figure 7. From this simulation, we determine that 60% of the total Ar remains trapped inside the TGO layers after 100 h. (Annealing at higher temperature is not considered as TGO films then show signs of crystallization [11]).

A striking feature in figure 8 is the considerable difference of Ar content in TGO layers compared to SiO_2. Moreover, the Ar content has increased in TGO and decreases in SiO_2 compared to the initial conditions, from 0.8% to 1% in TGO, and from 0.3% to about 0.15% in SiO_2. We find that the ratio of the amount of Ar in TGO compared to that in SiO_2 in the middle of the stack is about 7. This corresponds to the reciprocal of the ratio of the diffusion coefficients in the two materials, i.e. $e^{-1.2/kT}/e^{-1.35/kT} = e^{-0.15/kT}$, considering that the D_0 coefficients were set equal for both materials. Indeed, because the Ar diffuses 7 times more slowly in TGO than in SiO_2 at 600 °C, it spends more time in the TGO. The ratio is expressed as an orange line in the figure. At 450 °C, this ratio becomes even higher, at 11.

This could explain at least in part the behavior observed in figure 6(c): at 450 °C, the Ar diffuses very quickly in SiO_2 but slowly in TGO, and appears to accumulate in the latter. However, the concentration reached in this experiment is much higher than expected: if all the Ar in the SiO_2 ends up in the TGO, the concentration should reach about 1.2% rather than the 3.5% observed. We surmise that the extra Ar comes from deeper in the stack, through a process not considered in the model, with a stress profile due to difference in coefficient of thermal expansion (CTE) as a driver, for example. The model also does not explain the accumulation of Ar in the middle of the top SiO_2 layer.

A consequence of the PIXE and ERD-TOF results is that, in the end, the desorption process in 8.5 μm stacks is almost entirely controlled by the diffusion coefficient of TGO. The time to desorb the Ar can be computed as a few times $t = L^2/D_{\mathrm{TGO}}$ where L is the thickness of the stack. At 600 °C for a 8.5 μm stack, this corresponds to several weeks.

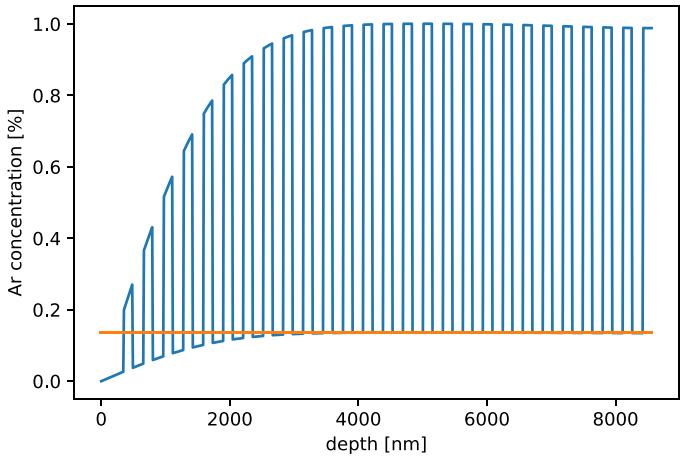

Figure 8. Blue curve: concentration of Ar as a function of depth in a 8.5 μm stack after a 10 h annealing at 600 °C, according to the transport model. Higher Ar amounts are found in the TGO layers while lower amount corresponds to the Ar content in SiO_2 layers. Orange line: ratio $D_{TGO}/D_{SiO_2} = 1/7.3$.

4. Stacks blistering

The problem that led us to investigate the Ar transport in TGO is that, during the course of the development of TGO/SiO_2 stacks as possible future Bragg mirrors for GWDs, we observed significant blistering upon annealing in such stacks after annealing at 600 °C for 10 h and 100 h. They were occurring at any depth in the stacks, sometimes with a small blister showing up on top of a bigger one, so it was clearly not just a problem with the stack adhesion on the substrate. The temperature at which these blisters appeared corresponds to the temperature at which Ar desorbs from TGO.

As mentioned, such long, high-temperature anneal is required to reach the performances needed in terms of low IMD [11]. The problem finally appeared to be mainly due to an elevated base pressure (2×10^{-6} Torr) in the deposition system, consisting of water vapor. Yet, such blistering is encountered from time to time during the annealing of deposited thin films and is worth understanding.

In this section, we present the analysis of movies shot during ramp anneals of different stacks deposited on standard-polished Corning 7980 fused silica samples and on Corning 7979 fused silica samples superpolished by Coastline Optics (RMS <0.1 nm). A blister growth model is developed to interpret these data. Two possible mechanisms are considered: blistering due to Ar desorption/accumulation, and stress-induced delamination.

4.1. Blister shape

Before we discuss the growth of such blisters, it is useful to characterize the shape they have. This is required to estimate their volume and therefore the amount of gas they contain, in the hypothesis that their growth is driven by Ar desorption. Using the setup described in section 2.5, we obtained such profiles for several blisters with a base radius ρ between 34 and 315 μm. Figure 9 shows the profile of three blisters (symbols). We see that their height h is a small fraction of their radius.

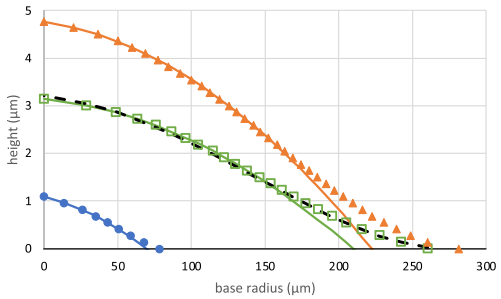

Figure 9. Measured profile (height as a function of the radius) of three different blisters (symbols) and fits of a circle (solid curves of the same color as the symbols) or the equation of a clamped circular plate under isostatic pressure (black dashed curve, fitted on the medium-sized blister.

They are fitted with a circle (solid colored lines) and one of them is also fitted with the equation for the deformation as a function of the radial coordinate r of a clamped circular plate on which a uniform pressure p is applied (black dashed curve):

$$h(r) = \frac{3}{16}\frac{p}{EL^3}\left(1-\nu^2\right)\left(\rho^2 - r^2\right)^2, \tag{7}$$

where E is the elastic modulus of the plate (which, for a stack, could be taken as the average over its thickness H), and ν is the Poisson's ratio. We see that the shape over about 70% of their radius is very well fitted by a circle, but the edges of the blisters do not break up abruptly as a truncated sphere would do. They rather have a smooth edge, much better represented by equation (7), which takes into account the mechanical properties of the film near the edge. Yet, this equation does not consider the peeling force involved during the growth of a blister. For now, we see that the spherical cap approximation gives a good estimate of the shape, and will make blister volume computation more compact. In any case, this experiment tells us that the blisters are fairly flat, and have a rather constant h/ρ ratio of $1.5 \pm 0.2\%$, independent of their size.

4.2. Filming and tracking blisters forming in stacks

Our setup, intended to measure light scattering as a function of temperature, can also be used to simply film the surface of a sample as it is annealed, as the sample being measured is illuminated by the heater rather than a laser. In the experiments described here, the temperature increased at a rate $R = 1\ ^\circ\mathrm{C\,min^{-1}}$. from 23 °C to 600 °C and the movies are shot at a rate of 20 frames $\mathrm{s^{-1}}$. Knowing the size of the field of view and the corresponding number of pixels, the area of several blisters is tracked as a function of time and temperature. The method applied to identify the blisters on each frame and measure their diameter is to use a template, which diameter is scanned from 10 to 90 pixels, and find the correlation of that template over each video frame. Typically, the correlation is high at several nearby points where a blister is located (i.e. points at a distance smaller than the diameter), so only the location with the maximum correlation is retained.

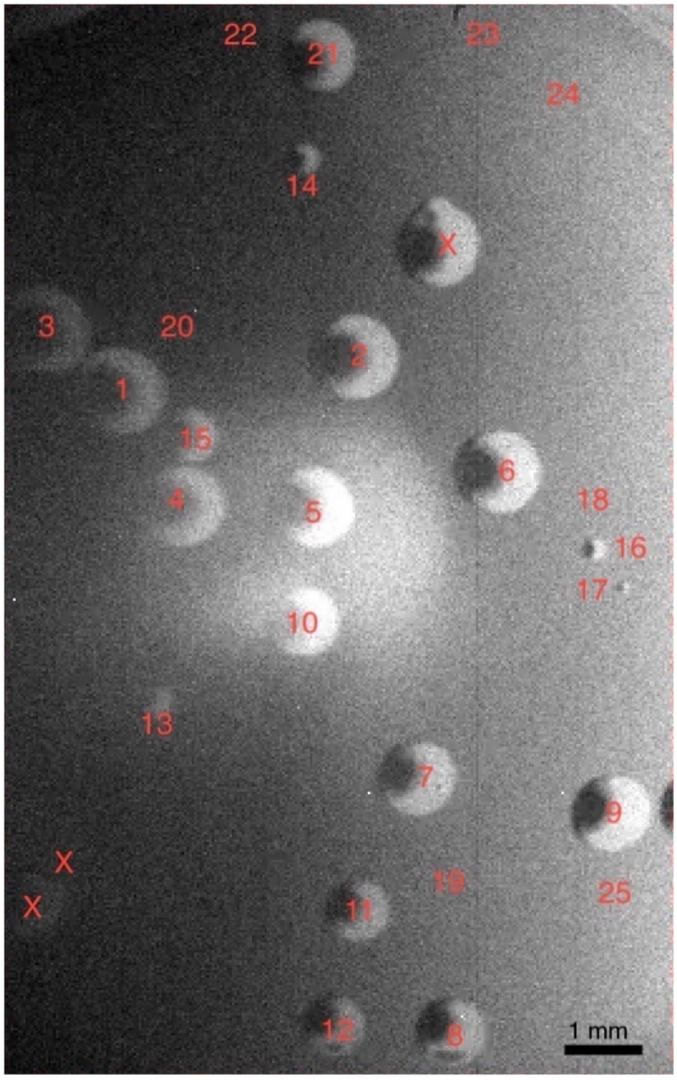

Figure 10. Video frame (at $T = 522$ °C) of blisters growing in the stack deposited on standard-polished fused silica. The 25 tracked blisters are identified by a number (including some that did not yet start to grow at that temperature yet), while a few that were not tracked are marked by an 'X'.

4.3. Blister growth

In the first experiment, on a stack deposited on standard-polished fused silica (deposition run #210811a), the first blister starts to grow at 495.5 °C. Each blister is tracked up to the video frame just before it touches another blister, this happens between 522 °C and 536° for most blisters. Given these data, at 536 °C, there are 28 blisters over an area of 0.65 cm^2, or 43 blisters cm^{-2}, and 25 of them are tracked. Their location is identified in figure 10, which shows a frame of the video at $T = 522$ °C.

When some blisters touch others, their growth slows down considerably. Under the assumption that the growth is driven by Ar accumulation, an area already covered by blisters accumulates the Ar underneath, and should mostly stop growing if neighboring areas had their Ar already accumulated in other blisters. In an alternative picture where blisters grow due to stress relaxation by delamination, blisters stop growing because stress is already released in neighboring areas. Past 536 °C, it becomes difficult to estimate the blister surface density, as several blisters undergo coalescence, and widespread buckling eventually occurs, see section 4.6.

Figure 11(a) shows the evolution of ρ for the blisters identified in figure 10 as a function of temperature. All blisters that start to grow below 512 °C (#1 to #12 and #21; group A) grow quickly at first, within 5 °C, up to a radius of about 300 μm, and then shift to a slower growth regime. Assuming a blister-nucleation-controlled process, it is as if there was a latent and supersaturated amount of Ar ready to join a blister, which happens quickly after a blister has nucleated, explaining the fast regime. Once the amount of detrapped Ar has reached equilibrium, the growth continues at a pace controlled by Ar detrapping. We see, however, that for most blisters, the radius increase is non-linear and accelerating during this second regime. For blisters starting to grow above 512 °C, the picture is more complex. Some blisters (#13, #14, #16, #22; group B) start growing at a slower rate than those of Group A, then accelerate, with #14 showing a growth rate that slows down just before touching another blister. Blister #13 shows the peculiar behavior that it stops growing at 537 °C, without touching other blisters. Other blisters (#15, #17, #18, #20, #23, #25; group C) only show a fast growth phase, at a rate similar to the one observed during the first phase for the blisters of Group A. Blister #24, which starts to grow at a relatively high temperature in an isolated area, shows a surprisingly slow initial growth compared to the other blisters. It then accelerates more or less continuously, reaching a growth rate comparable to that of the other blisters. The mean radius of the tracked blisters before they touch another one is 600 μm. Those of Group A average at 700 μm.

4.4. Volume and pressure estimates

In the hypothesis according to which the blister growth is driven by Ar desorption, we are interested in the volume of the blisters in order to estimate the amount of gas they contain. We consider that the blisters have the shape of a spherical cap (despite the smoothness of their edges, which should contribute only a small extra volume) and we have observed that their height remains a constant fraction f of the radius ρ of their base, with $f = 1.5\%$. The volume of a truncated sphere is given by:

$$V = \frac{\pi}{6}\rho^3\left(3f+f^3\right) \approx \frac{\pi}{2}f\rho^3,\ f \ll 1. \tag{8}$$

Figure 11(b) presents in an Arrhenius plot the evolution of the volume computed using equation (8). Indeed, if blister growth is driven by thermal desorption of the Ar, their volume might be related to the Boltzmann factor of that process. In that representation of the data, the second growth regime appears relatively straight for most blisters of Group A. The effective activation energy related to this process is very high, however, and probably meaningless, as we will discuss below. The figure shows that for the blister of Group A, the final average volume is 9 nL. The median volume of all the blisters tracked is 4.4 nL and ranges between 0.3 and 30 nL for a total volume of 170 nL.

Based on those quantities, we then estimate how much Ar the blisters contain. The total thickness of the stack is about 8.5 μm. The density of TGO is 7×10^{22} at cm^{-3} and that of SiO_2 typically 6×10^{22} at cm^{-3}. They initially contain respectively about 0.8% and 0.3% Ar.

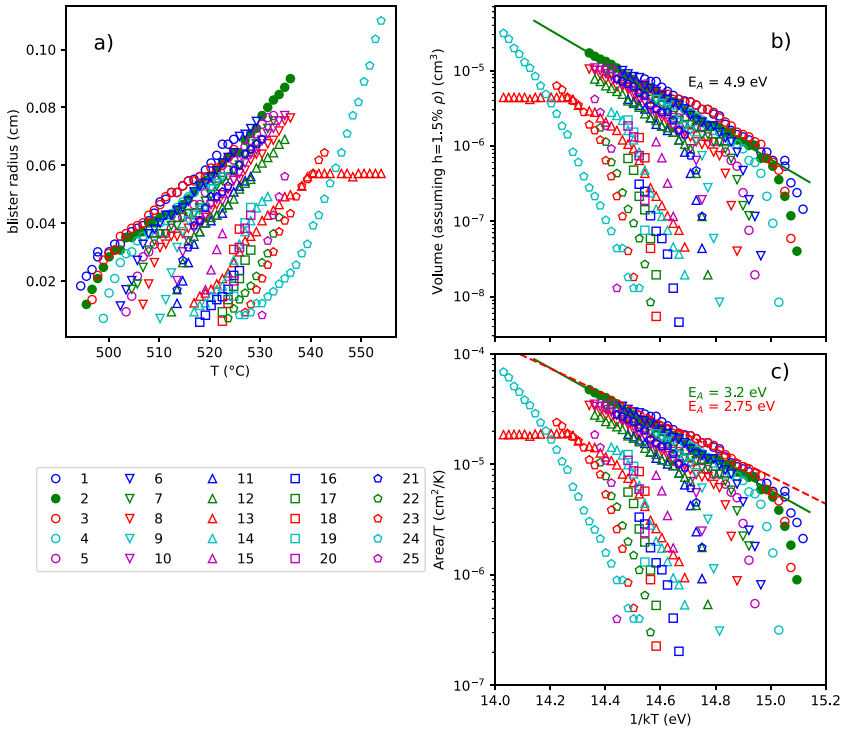

Figure 11. For the 25 blisters identified in figure 10, (a) base radius ρ as a function of temperature, (b) Arrhenius plot of the blister volume (equation (8) with $f = 1.5\%$), and (c) Arrhenius plot of the blister area divided by temperature (equation (14)). The green curve is an Arrhenius relation fitted on the data represented by filled green circles (blister #2). The red dashed one corresponds to equation (17).

The total Ar areal density in the complete 52-layer stack is therefore approximately 3.2×10^{17} Ar/cm^2. If we consider an average blister of Group A, with a volume $V = 9$ nL, the radius of such blisters is 714 μm according to the reciprocal of equation (8). The area it covers on the substrate is therefore 0.016 cm^2, with $N = 5 \times 10^{15}$ Ar atoms underneath. If we assume that all Ar under such a blister found its way inside it, $N/V = 6 \times 10^{20}$Ar/cm^3. This is a density low enough to use the ideal gas law:

$$p = \frac{N}{V} k_\mathrm{B} T. \tag{9}$$

At $k_\mathrm{B}T = (1/14.4)$ eV, we get $p = 6.7$ MPa. While being a relatively high pressure for a gas, this is a relatively low value compared to typical mechanical stresses. If we rather consider the total area of the blisters, 0.31 cm^2, and the total volume, 170 nL, we also get 6.6 MPa.

We note that we assume that all Ar made its way into the blister. We ignore if the amount of Ar remaining in the stack is significant, and if some Ar may have desorbed to the surface rather than inside blisters. So this estimate is a maximum boundary for pressure. Also, the growth is not completely stopped yet at the point for which we carry these calculations. On the one hand, not all Ar might have diffused, and further diffusion into the blisters may explain the remaining slow growth. On the other hand, T continues to increase, increasing pressure (equation (9)) and promoting further blisters expansion.

4.5. Considering the tension in the membrane

Two points we have not considered so far are the effect of temperature on pressure (except for the pressure estimate we just discussed) and the fact that the membrane (i.e. the outer shell of a blister) exerts an elastic force that translates into an increased pressure inside the blisters. Laplace relation predicts that the pressure, p inside a bubble of radius r under surface tension σ compared to the outside pressure p_0 is given by:

$$p - p_0 = \frac{2\sigma}{r}. \tag{10}$$

In this expression, the radius of curvature r differs from ρ, the radius of the blister base. They are related through f as follows:

$$(r - f\rho)^2 + \rho^2 = r^2, \tag{11}$$

so

$$r = \frac{f + 1/f}{2}\rho. \tag{12}$$

Let us assume that the blisters form because gas molecules diffuse and nucleate somewhere between the layers of the stack (perhaps at an imperfection or impurity), and that the top layers form an elastic membrane. Since detrapping or diffusion are thermally activated processes and we are to estimate the activation energy of the limiting process, we need to express the quantity that evolves with temperature including effects such as Laplace relation. We may either consider that the layer forming the blister membrane has an elastic constant from which we can deduce σ, or that the blister membrane is attached all around to the next layer or the substrate by a peeling force equivalent to a surface tension σ. At any reasonable pressure (i.e. $N/V \ll 10^{22}\text{at}\,\text{cm}^{-3}$ so ideal gas law applies) and considering $p \gg p_0$, the number N of gas molecules in the blister according to equation (9) should go as:

$$N = \frac{2\sigma}{1 + 1/f^2}\frac{\pi\rho^2}{k_\text{B}T}, \tag{13}$$

where we replaced V by the approximate term of equation (8), p by equation (10), and in that, r from equation (12). From that, we get

$$\frac{\pi\rho^2}{T} = k_\text{B}\frac{1 + 1/f^2}{2\sigma}N. \tag{14}$$

Hence, if the blister membrane shows some elasticity or peeling force, and if that elasticity is constant or if the peeling force is constant, a plot of $\pi\rho^2/T$ should scale with the amount of Ar trapped in a blister, which should be proportional to the amount of Ar that was able to diffuse. This is what figure 11(c) shows. In that graph, a fit on the data represented by the filled green circles (blister #2) features an 'effective' activation energy of about 3.2 eV.

In section 3.2, assuming a detrapping-limited desorption process, we found an activation energy $E_\text{A} = 2.75$ eV, but that was deduced from isothermal annealing rather than a ramp anneal as it is the case here. Solving equation (1) for $T = Rt + T_0$, we find

$$N = N_0\left(1 - \exp\left(C\left[xe^{1/x} - Ei\,(1/x)\right]\right)\right), \tag{15}$$

where

$$x = -\frac{E_\text{A}}{k_\text{B}\,(Rt + T_0)}, \quad C = \frac{\nu_0 E_\text{A}}{k_\text{B}R}, \tag{16}$$

and $Ei(z)$ is the exponential integral function. Replacing N in equation (14), we should have

$$\frac{\pi\rho^2}{T} = \underbrace{k_B \frac{1+1/f^2}{2\sigma} N_0}_{B} \left(1 - \exp\left(C\left[xe^{1/x} - Ei\left(1/x\right)\right]\right)\right). \tag{17}$$

This expression is plotted as a red dashed curve in figure 11(c), with the factor $B = 6 \times 10^{-4}$ cm^2 K^{-1}. Assuming that $N_0 = 5 \times 10^{15}$ as we estimated above for an average blister of Group A, it yields a $\sigma = 2600$ N m^{-1} or, assuming a 'membrane' thickness of 8.5 μm (i.e. the stack thickness), a modulus of 330 MPa. Interestingly, this value corresponds to the tensile strength of TiO_2 [31]. It can be argued that not all the Ar reaches a blister, so we might consider a lower value for N_0, but we can also see from figure 11(c) that we could have selected a lower value of B to better fit the behavior of other blisters. The value of σ remains of the right order of magnitude compared to values of yield or tensile strength observed in such materials.

4.6. Buckling

We mentioned at the beginning of this section that another hypothesis to explain the blistering process is delamination, which allows the relaxation of stress resulting for example from the difference in the CTE of TGO compared to SiO_2. Indeed, the latter has a CTE of 0.38×10^{-6} K^{-1} [32], while germania has a CTE of 7.7×10^{-6} K^{-1} [33] and titania has one of 2.57×10^{-6} K^{-1} [32]. Delamination also depends on the nucleation of the buckling at some imperfection of impurity. From that point of view, the first growth regime would be due to a rapid release of the accumulated elastic energy, and the second growth regime (observed especially for blisters of Group A) would result from the still-expending TGO. However, in their review paper, Hutchinson and Suo [34] estimate the spallation time in the sub-second regime, typical of crack propagation and much shorter than the growth timescale observed for the 25 blisters we tracked even during their fast growth regime.

Then, we also observed some oddly shaped blister suddenly popping up in the spaces remaining around the already-grown blisters at a temperature of 563 °C. Most of them grow to their final size between two frames (<1 min.). We note that this corresponds to the temperature at which the CTE of $Ti_{0.127}Ge_{0.873}O_2$ starts to increase abruptly, according to Kamiya and Sakka [35] .

This effect is visible when looking closely at two successive frames. Figure 12 shows two consecutive images in a particular location of the field of view. The top row shows the images themselves, where blisters that are initially not present (or just starting to appear) are pointed by arrows. The ones pointed by green arrows are not visible in the left image but are in the right image. This is the case of most blisters that grow during that phase: they pop up within a single image interval. Those pointed by red arrows are already present in the left image, but with a much lower contrast, and reach their final aspect in the image on the right. At least two interpretations can be considered for the latter:

- the blisters have grown over a 2-frame, ∼2 °C interval
- they popped up during the exposure time of the left image so what we see for those blisters is actually a superposition of the darker background and the fully grown blisters as it appears in the right image. Indeed, only about 10% of those blisters can be seen growing on two consecutive frames.

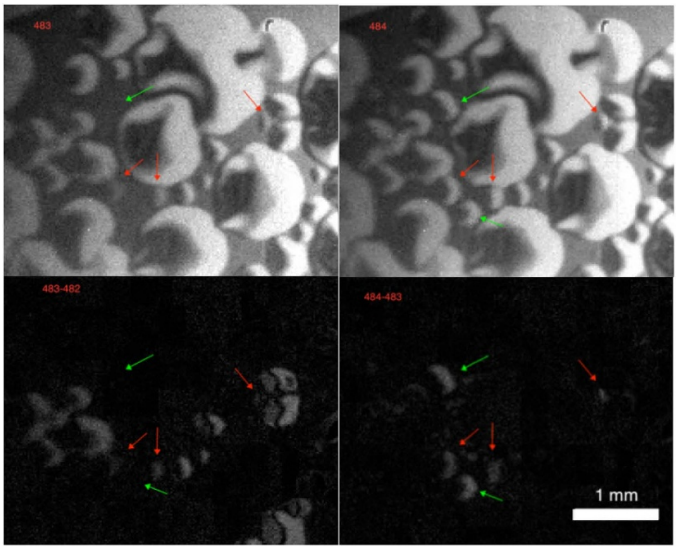

Figure 12. Top row: two consecutive frames (1 min, ∼1 °C difference) near 565 °C. Blisters popping up between these two images are indicated by a green arrow, while those growing over two frames are pointed by red arrows. Bottom row: the images on the top row subtracted by their previous image.

In any case, the growth of these blisters occurs on a short time interval, which is compatible with a delamination that relieves the stress in the film.

4.7. Super-polished substrate

Whether blister growth is driven by Ar desorption or delamination, both processes need a nucleation site to occur. If nucleation is a factor, it might originate from the substrate. To check this hypothesis, another ramp anneal experiment was conducted on a stack deposited on an super-polished fused silica substrate (deposition run #PL014). Unfortunately, during the experiment, a technical problem stopped the ramp, which restarted automatically at 576 °C, while erasing previous data.

The video, which covers the ramp from 576 °C to 600 °C and then the soak at that temperature, was analyzed following the same method as described in section 4.3. Results are presented in figure 13: panel (a) shows the blisters that are tracked. Actually, many small blisters just appear and do not further increase in size, so they are not tracked. In (b), we plot the radius as a function of temperature. Data below 576 °C are not available but it is clear that the data are not in continuation of those presented in figure 11(grey data points). They all appear to show only the fast growth regime, with a similar slope, until many of them stop growing. A few actually decapsulate at some point. Figure 13(c) shows the data represented according to equation (17), but the slope is too steep to be modeled by any reasonable activation energy. It is therefore not clear if the process is driven by a supersaturation of Ar, which should all be detrapped at such temperature, or if it is driven by stress relaxation, although the process occurs over a few minutes, much longer than typical times for crack propagation.

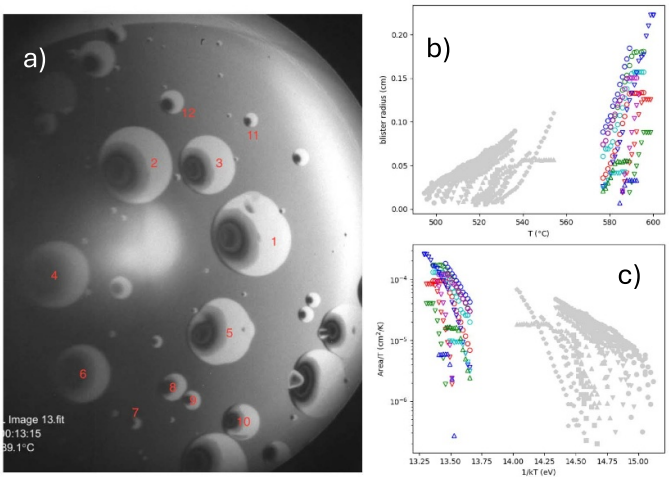

Figure 13. (a) Image of sample PL014 on which tracked blisters are identified. (b) Radius evolution as a function of temperature. The data presented in figure 11(a) are plotted in grey for reference. (c) Arrhenius plot of $\pi\rho^2/T$ for each tracked blister between 576 °C and 600 °C. The data from figure 11(c) are plotted in grey for reference.

4.8. Stress relaxation vs. Ar desorption: step-annealing

In order to distinguish between the two mechanisms, we carried out the following experiment with another stack also deposited on super-polished silica (deposition run #PL020): if we stop the ramp and hold the temperature during blister growth, this would stop thermal expansion, hence blister growth, if stress relaxation by delamination is the driving mechanism. If Ar release is the driver, the blister should continue to grow, since Ar desorption is still going on.

Indeed, in a case where the heating ramp is stopped at time t_s, at a temperature between 495 °C and 563 °C, equation (15) tells us the amount of gas remaining, N_s. According to equation (1), the characteristic time τ needed to desorb this remaining amount of Ar during such an isotherm should be given by :

$$\frac{1}{\tau} = \nu \exp\left(-\frac{E_\mathrm{A}}{k_\mathrm{B}\left(Rt_s + T_0\right)}\right). \tag{18}$$

If we consider for example $Rt_s + T_0 = 500$ °C and $E_\mathrm{A} = 2.75$ eV, $\tau = 11$h. At 530 °C, $\tau =$ 2.4 h. The growth should therefore be relatively slow.

During this experiment, the temperature was increased to 500 °C at 1 °C min^{-1}, and then held at that temperature for 1 h, followed by an increase of 10 °C at 1 °C min^{-1} and held for 1 h at 510 °C, and so on until the temperature reached 600 °C. We note that, being a stack deposited on an super-polished silica substrate, we expect blister formation as in the experiment described in section 4.7, showing only the fast growth regime, and not necessarily the slow growth regime observed for Group A blisters in figure 11.

Results are presented in figure 14. The top panel indicates the blisters that are tracked. (Blister #0, near the center, is an example of wrong identification, so results have to be inspected.) As for the experiment reported in section 4.7, many small blisters just pop up and do not further change in size; those were left out from figure 14(b) for clarity, which show the blister diameter (in pixels) as a function of time. The blister identification number appears to the left

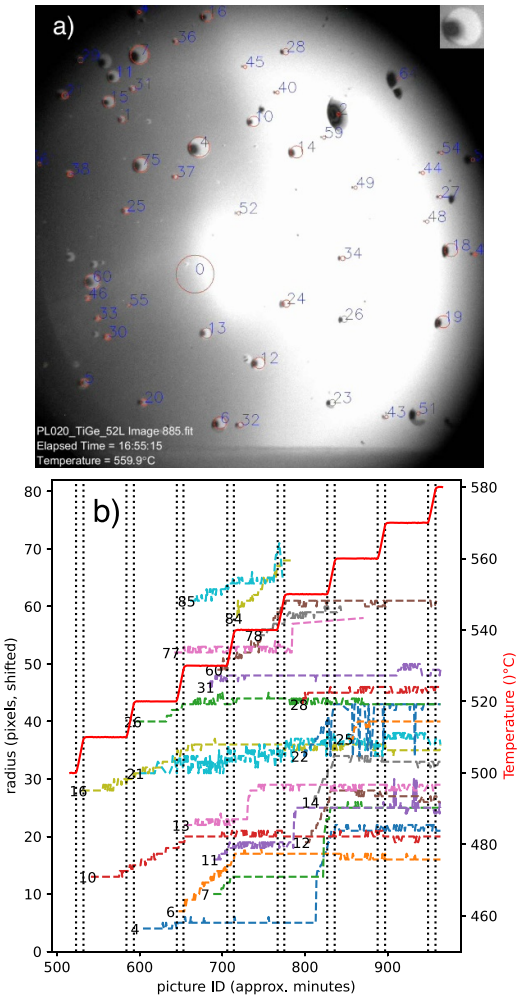

Figure 14. (a) Image of sample #PL020 on which automatically tracked blisters are identified. Inset top right: blister template (see text). (b) Radius evolution as a function of frame number (approximately minutes) for a number of blisters. Data are shifted vertically for clarity. The number left of the place where each curve starts indicates the blister identification number. The red curve represents the temperature against the right axis. The plateaus are 1 h long and the temperatures ramps 10 min. long. The transitions from a plateau to a ramp and inversely are indicated by vertical dotted lines.

of the beginning of each curve. The curves are shifted for clarity, but most started to be tracked at a radius of about 4 pixels. The temperature is plotted in red against the right axis.

While the growth is often discontinuous, we see from this graph that no blister grows only during the temperature ramps. Part of the blisters finish growing at the end of a plateau, but do not grow further at the next temperature ramp. Since the growth does not stop during the plateaus, and growth is observed during the 1 h-timescale of a plateau, the Ar-driven mechanism hypothesis should be favored.

Figure 15 shows a subset of the curves present in figure 14(b), this time not shifted so they can be directly compared. We see on this graph that during plateaus, the slope of the curves

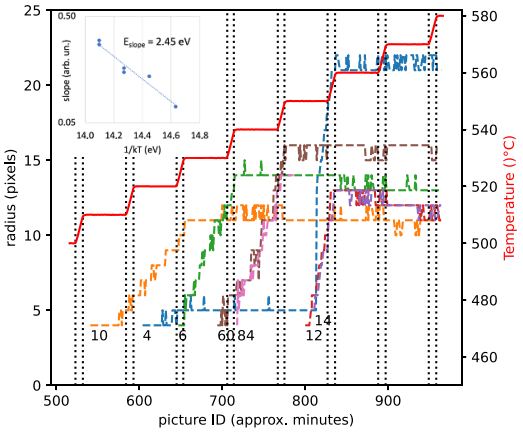

Figure 15. Subset of the curves plotted in figure 11(b), now unshifted. The red curve represents the temperature, plotted against right axis. Inset: Arrhenius plot of the growth slope.

increases when the growth occurs at higher temperature. For example, the growth of blister #10 spans more than 1 h, while that of #12 lasts about 20 min. The inset of figure 15 is an Arrhenius plot of these slopes. It featuring an effective activation energy of 2.45 eV, not too far from the value of 2.75 eV found for detrapping.

There are therefore many results at this point that favor a model where blister growth is driven by Ar detrapping. However, it is clear from the annealing experiments conducted on stacks deposited on 'standard-polished' substrates (section 4) compared to those carried out on stacks deposited on super-polished substrates (sections 4.8 and 4.7) that nucleation is the limiting or determining factor, at the origin of the unpredictable behavior of blister growth, which starts at various temperatures between 500 °C and 600 °C, and grow up to arbitrary sizes, sometimes restarting to grow afterwards. It appears clear that the process is influenced or controlled by many factors. Yet, we now know that water vapor was a major player, as mentioned in introduction and section 4. We surmise that it affects the layers adhesion, enabling the blistering process to occur, while Ar release seems to be the driver for their growth. It underlines the importance of a good base pressure in deposition systems to avoid contamination.

5. Conclusion

Blistering is a phenomenon sometimes observed during the annealing of thin films, but the origin of the process is not always investigated in depth, a solution to avoid it rather being sought by a better control of the process. Here we considered the case of a TGO/SiO_2 stack, which is a candidate for Bragg mirrors in GWDs because TGO has a relatively high refractive index and a low loss angle if annealed at 600 °C for 100 h. Blisters appeared in some of the 52-layers, 8.5 μm TGO/silica stacks during such anneal, at a temperature that corresponds to the range where Ar desorbs from the TGO. While the effect has been mitigated primarily through the reduction of H_2O partial pressure during TGO/silica stacks growth, in order to understand better the role of Ar in the blistering process, we investigated the transport of Ar in single layers, and applied it to stacks. We can model reasonably well the evolution of Ar depth profiles in TGO single layers with an activation energy for detrapping of 2.70 eV considering a attempt frequency of $\nu_0 = 10^{13}$ and an activation energy of 1.35 eV for diffusion assuming

a prefactor of 9×10^{-6} cm^2 s^{-1}. In the case of <1 μm-thick layers, the desorption process is mainly limited by detrapping. The Ar transport model also correctly predicts the evolution of the total amount of Ar in a 8.5 μm stack annealed at 450 °C, but in that case, the process is mainly limited by diffusion. The transport model explains the Ar accumulation in TGO as a result of slower diffusion in that material compared to silica. It can be applied to explain some regimes of the blisters growth, and we find indications that Ar accumulation is a driver for their growth in general, but the blisters nucleation and growth remains a complex phenomenon influenced by several other factors.

Data availability statement

The data are in various forms and require explanations accompanying them. The data that support the findings of this study are available upon reasonable request from the authors.

Acknowledgments

The work performed at UdeM and Polytechnique Montréal was supported by the Natural Sciences and Engineering Research Council of Canada (NSERC), the Canadian foundation for innovation (CFI) and the Fonds de recherche Québec, Nature et technologies (FQRNT) through the Regroupement Québécois sur les Matériaux de Pointe (RQMP), as well as a Projet de coopération Québec-Wallonie-Bruxelles (Wallonie: #RECH-INNO-02, Québec: #11.802). The authors thank Prof. S Roorda and F Debris from U Montréal for fruitful discussions and technical support. Cal State Fullerton authors were supported by NSF Awards PHY-2207998 and PHY-1807069, the Dan Black Family Trust, and Nancy and Lee Begovich. The authors thank their colleagues within the LIGO Scientific Collaboration for advice and support. LIGO was constructed by the California Institute of Technology and Massachusetts Institute of Technology with funding from the National Science Foundation, and operates under cooperative Agreement PHY-0757058. Advanced LIGO was built under Award PHY-0823459. This paper has LIGO Document Number LIGO-P2300328.

ORCID iDs

Annalisa Paolone https://orcid.org/0000-0002-4839-7815
Marco Bazzan https://orcid.org/0000-0002-1451-1368
Martin Chicoine https://orcid.org/0000-0003-0630-3996
Julien L Colaux https://orcid.org/0000-0002-8940-2991
Ludvik Martinu https://orcid.org/0000-0003-2630-4048
Carmen Menoni https://orcid.org/0000-0001-9185-2572
Christophe Michel https://orcid.org/0000-0003-0606-725X
Fulvio Ricci https://orcid.org/0000-0001-5475-4447
François Schiettekatte https://orcid.org/0000-0002-2112-9378
Joshua R Smith https://orcid.org/0000-0003-0638-9670
Gabriele Vajente https://orcid.org/0000-0002-7656-6882

References

[1] Gulden M 1967 *J. Nucl. Mater.* **23** 30
[2] Skinner C H *et al* 2008 *Fusion Sci. Technol.* **54** 891

[3] Terreault B 2007 *Phys. Status Solidi* a **204** 2129
[4] Aspar B *et al* 1997 *Microelectron. Eng.* **36** 233
[5] Moutanabbir O, Terreault B, Chicoine M, Schiettekatte F and Simpson P J 2007 *Phys. Rev.* B **75** 075201
[6] Schiettekatte F, Wintgens C and Roorda S 1999 *Appl. Phys. Lett.* **74** 1857
[7] Araiza J d J, Álvarez Fraga L, Gago R and Sánchez O 2023 *Materials* **16** 5331
[8] Zhao S, Yuan G, Zhang Di, Xu P, Li G and Han W 2021 *J. Mater. Sci.* **56** 17478–89
[9] Guo T *et al* 2017 *Acta Mater.* **138** 1
[10] Hatton P, Goddard P, Smith R, Abbas A, Potamialis C, Greenhalgh R and Walls J M 2019 *Thin Solid Films* **692** 137614
[11] Vajente G *et al* 2021 *Phys. Rev. Lett.* **127** 071101
[12] Aasi J *et al* 2015 *Class. Quantum Grav.* **32** 074001
[13] Acernese F *et al* 2015 *Class. Quantum Grav.* **32** 024001
[14] Abbott B P *et al* 2016 *Phys. Rev. Lett.* **116** 061102
[15] Abbott B P *et al* 2017 *Phys. Rev. Lett.* **119** 161101
[16] Fritschel P *et al* (LIGO Scientific Collaboration) 2024 *LSC Instrument Science White Paper* (California Institute of Technology and Massachusetts Institute of Technology)
[17] Callen H B and Welton T A 1951 *Phys. Rev.* **83** 34
[18] Levin Y 1998 *Phys. Rev.* D **57** 659
[19] Davenport A *et al* 2022 The development of high reflection TiO2:GeO2 and SiO2 coatings for gravitational wave detectors *Optical Interference Coatings Conf. (OIC) 2022* (Optica Publishing Group) p WA.6
[20] Rezac M, Martinez D, Gleckl A and Smith J R 2023 *Appl. Opt.* **62** B97
[21] Mayer M 1999 *AIP Conf. Proc.* **475** 541–4
[22] Chicoine M, Schiettekatte F, Laitinen M and Sajavaara T 2017 *Nucl. Instrum. Methods Phys. Res.* B **406** 112
[23] Schiettekatte F, Chicoine M, Gujrathi S, Wei P and Oxorn K 2004 *Nucl. Instrum. Methods Phys. Res.* B **219–220** 125
[24] Campbell J L, Hopman T L, Maxwell J A and Nejedly Z 2000 *Nucl. Instrum. Methods Phys. Res.* B **170** 193
[25] Gurbich A 2016 *Nucl. Instrum. Methods Phys. Res.* B **371** 27
[26] Demarche J, Yedji M and Terwagne G 2010 *Nucl. Instrum. Methods Phys. Res.* B **268** 2107
[27] Gupta D 2005 *Diffusion Processes in Advanced Technological Materials* (Springer Science & Business Media)
[28] Perkins W G and Begeal D R 2003 *J. Chem. Phys.* **54** 1683
[29] Abernathy M *et al* 2021 *Class. Quantum Grav.* **38** 195021
[30] Schiettekatte F 2014 *Nucl. Instrum. Methods Phys. Res.* B **332** 404
[31] Materials A Properties: Titanium Dioxide—Titania (TiO2) (available at: www.azom.com/properties.aspx?ArticleID=1179) (Accessed 01 September 2023)
[32] Lee C-C, Tien C-L, Sheu W-S and Jaing C-C 2001 *Rev. Sci. Instrum.* **72** 2128
[33] Dianov E and Mashinsky V 2005 *J. Lightwave Technol.* **23** 3500
[34] Hutchinson J and Suo Z 1991 *Mixed Mode Cracking in Layered Materials* (*Advances in Applied Mechanics* vol 29) (Elsevier) pp 63–191
[35] Kamiya K and Sakka S 1982 *J. Non-Cryst. Solids* **52** 357